Stable Cycle Performance of Phosphorus Negative Electrode in Lithium-Ion Batteries Derived From Ionic Liquid Electrolytes

Shubham Kaushik, Kazuhiko Matsumoto, Rika Hagiwara*

Graduate School of Energy Science, Kyoto University, Sakyo-ku, Kyoto 606-8501, Japan

*Corresponding Author E-mail Address: k-matsumoto@energy.kyoto-u.ac.jp

Keywords: Ionic liquid electrolyte, phosphorus based negative electrode, solid electrolyte interphase, full-cell

Abstract

Although high-capacity negative electrode materials are seen as a propitious strategy for improving lithium-ion battery (LIB) performance, their advancement is curbed by issues such as pulverization during charge-discharge and the formation of unstable solid electrolyte interphase (SEI). In particular, electrolytes play a vital role to determine the properties of SEI layer. Thus, in this study, we investigate the performance of a red phosphorus/acetylene black composite (P/AB) prepared by high energy ball-milling as a negative electrode material for LIBs using organic and ionic liquid (IL) electrolytes. Galvanostatic tests performed on half cells demonstrate high discharge capacities in the 1386–1700 mAh $(g\text{-}P/AB)^{-1}$ range along with high Coulombic efficiencies of 85.3–88.2 % in the 1st cycle, irrespective of the electrolyte used. Upon cycling, the Li[FSA]-[C_2C_1im][FSA] (FSA^- = bis(fluorosulfonyl)amide and $C_2C_1im^+$ = 1-ethyl-3-methylimidazolium) IL electrolyte (2:8 in mol) demonstrates a high capacity retention of 78.8% after 350 cycles, whereas significant capacity fading is observed in the Li[PF_6] and Li[FSA] organic electrolytes. Electrochemical impedance spectroscopy conducted with cycling revealed lower interfacial resistance in the IL electrolyte than in the organic electrolytes. Scanning electron microscopy and X-ray photoelectron spectroscopy after cycling in the different electrolytes evinced that the IL electrolyte facilitates the formation of a robust SEI layer comprising multiple layers of sulfur species resulting from FSA^- decomposition. A P/AB|$LiFePO_4$ full-cell using the IL electrolyte showed superior capacity retention than organic electrolytes and a high energy density under ambient conditions. This work not only illuminates the improved performance of a phosphorous-based negative electrode alongside ionic liquid electrolytes but also displays a viable strategy for the development of high performance LIBs especially for large-scale applications.

1. Introduction

Lithium-ion batteries (LIBs) have become the choice energy storage system for numerous applications ranging from electric vehicles to grid storage on account of their high energy and power densities.[1-2] Despite this prominence, the expansion of LIB technology is greatly impeded by scarcity of sustainable components leading to deficiencies such as low reversible capacity, poor safety and high cost.

In an effort to address these challenges, the search for viable negative electrodes remains a focal area of LIB development. Graphite negative electrodes remain widely utilized in contemporary LIB configurations despite their constrained theoretical capacity of 372 mAh g^{-1} engendered by limited Li intercalation in their charged state.[3-4] Similarly, other carbonaceous alternatives such as nitrogen-doped carbon nanotubes and hard carbons have been reported to deliver limited reversible capacities of 270 mAh g^{-1} and 300–530 mAh g^{-1}, respectively.[5-7] Comparatively, alloy-based negative electrode materials have displayed high reversible capacities (e.g. 990 mAh g^{-1} for $Li_{4.4}Sn$, 1625 mAh g^{-1} for $Li_{4.4}Ge$, and 3579 mAh g^{-1} for $Li_{3.75}Si$) due to their high Li intake capabilities during alloying processes.[8-11] However, it should be noted that despite their large capacities, the high Li intake often causes massive volume changes during battery operations leading to pulverization of active materials, unfavorable side reactions and capacity degradation.[12-13]

Phosphorus-based materials have also drawn considerable attention as negative electrode materials owing to their high theoretical capacities (~2596 mAh g^{-1}) and abundant resources.[14-15] However, low electrical conductivity (~10^{-14} S cm^{-1}) and large volume changes during charging and discharging heavily afflict their practicality. As a solution, carbon composite P (P/C) has been employed to increase electrical conductivity and mitigate the massive volume changes.[16-17]

Likewise, imbedding red P into conductive carbon nanostructures such as nanospheres or nanofibers has also been found to bring out high cycleability and rate capability in this class of materials.[18-19] However, noteworthy drawbacks to this approach include; increased electrolyte decomposition caused by the large surface area of the nanostructures and reduced tap density due to the high porosity of the resulting composite electrodes. Furthermore, the complex synthesis processes involved inhibit the scalability of nanostructured P/C composites. Therefore, for the sustainability of these materials, a facile method is required to synthesize P/C composite particle sizes in the sub-micrometer to micrometer range.

In 2007, one of the earliest studies involving black P/Super P (70:30 wt%) composite prepared by the high energy ball-milling (HEBM) method reported a high discharge capacity of 1814 mAh g^{-1} in the first cycle.[20] However, for a stable cycle performance, the voltage range was narrowed from 0.0 – 2.0 V to 0.78 – 2.0 V resulting in a lower reversible capacity of 600 mAh g^{-1}. Multi-walled carbon nanotubes (MWCNT) have also been actively investigated as the carbon source for the P/C composite.[21-22] Incorporating MWCNT into the P/C composite through physical and chemical imbedding was found to not only improve electrical conductivity but also suppressed the pulverization of red P.[23] Other carbon materials such as graphite [24-25], graphene [26], reduced graphene oxide [27], and acetylene black (AB) in P/C composite have also been found to facilitate high electrochemical performance. A red P/reduced graphene oxide (70:30 wt%) nanohybrid prepared by a hydrothermal method provided a high reversible capacity of 1600 mAh g^{-1} in the first cycle discharge process retaining a capacity of 1000 mAh g^{-1} after 80 cycles.[28] In another study, a red P/graphene (80:20 wt%) composite synthesized by ultrasonication demonstrated a capacity retention of 1286 mAh g^{-1} after 100 cycles and high rate capability.[29] Table 1 summarizes the electrochemical performance of previously reported P/C composite negative electrode

materials for LIBs.

Electrolyte choice remains an essential part of LIB development as it determines critical factors such as electrochemical stability, ion transport, and safety.[30] In commercial LIBs, carbonate-based organic electrolytes have shown high susceptibility to fire hazards due to their high flammability and volatility.[31-32] Consequently, ionic liquid electrolytes (ILs) have emerged as safer alternatives by virtue of their low flammability, negligible volatility, high thermal stability, and wide electrochemical window.[33-36] Besides, ILs manifest superior electrochemical performance compared to their organic counterparts due to their benign solid-electrolyte interphase properties (SEI layer) and high ionic conductivities.[37-38]

A robust SEI layer is particularly vital for alloy-based negative electrodes because of the stresses induced by large volume changes during charge/discharge processes. In a comparative study on the SEI layer properties of a Si negative electrode in IL and organic electrolytes, the SEI layer formed in the Li[FSA]-[C_3C_1pyrr][FSA] (FSA = bis(fluorosulfonyl)amide, C_3C_1pyrr = *N*-methyl-*N*-propylpyrrolidinium) IL electrolyte was found to be more stable compared to $LiPF_6$-EC:DEC organic electrolyte owing to the different chemistries of the component species (i.e. SEI formed in IL was composed of LiF, sulfur, and oxygen species whereas $LiPF_6$-EC:DEC mostly contained organic molecules), leading to better cycleability in the IL electrolyte.[39] Moreover, the full-cell constructed with Si/IL/Li($Ni_{1/3}Mn_{1/3}Co_{1/3}$)O_2 sustained a high capacity retention for 1000 cycles. Remarkable electrochemical performances have also been noted among other negative electrodes such as Sn/C,[40] TiO_2,[41] and graphite,[42] in ILs.

Among commonly utilized ILs, pyrrolidinium-based ILs are more actively investigated compared to imidazolium-based ILs, despite the latter generally exhibiting higher ionic conductivities and lower viscosities that enable faster charging and discharging.[43-44] A previous

investigation into the thermal, physical, and electrical properties of the Li[FSA]-[C_2C_1im][FSA] ($C_2C_1im^+$ = 1-ethyl-3-methylimidazolium) IL showed high thermal stability, a wide electrochemical window (~5.1 V), and high ionic conductivity of 10.1 mS cm^{-1} at 25 °C for Li[FSA]-[C_2C_1im][FSA] (2:8 mol).[33] Additionally, another recent study on Li metal batteries revealed effective dendrite suppression during Li metal deposition in this IL at both 25 and 90 °C, achieving high cycleability in full-cell configuration evincing this IL as a promising candidate for safer and long-lasting batteries.[45]

In sodium-ion batteries (NIBs), a red P/AB composite (AB~32 wt%) prepared by ball-milling showed a significant improvement in capacity retention when used with an IL electrolyte as opposed to organic electrolytes due to the formation of a uniform and robust SEI layer in the IL.[46] Despite the improved efficacy, the electrochemical performance of red P/AB composites with IL electrolytes in LIBs remains vastly unexplored, with no existing literature to our knowledge.

Thus, this study reports a comprehensive investigation on the performance of a red P/AB (6:4 w/w) composite prepared by HEBM as a negative electrode material for LIBs. The material is characterized using X-ray diffraction (XRD), scanning electron microscopy (SEM), energy-dispersive X-ray spectroscopy (EDX), Raman spectroscopy, and X-ray photoelectron spectroscopy (XPS). Half cells, full cells utilizing $LiFePO_4$ positive electrodes, as well as three-electrode cells, were assembled to evaluate the electrochemical performance of the negative electrode in selected organic electrolytes and two different concentrations of Li[FSA]-[C_2C_1im][FSA] (2:8 and 5:5 mol ratio) IL electrolytes. The 5:5 mol ratio is used because ILs with high Li salt concentrations showed superior interfacial properties to those with low or moderate concentrations. [47-48] Moreover, electrochemical impedance spectroscopy (EIS), XPS and SEM were used to elucidate the evolution of interfacial properties in respect to cycling the P/AB electrode in organic and IL

electrolytes. The charge-discharge mechanism is investigated using ex-situ XPS and XRD.

2. Experimental Section

2.1 Materials handling and preparation

All the air-sensitive materials were handled in a glove box (Miwa Manufacturing Co., Ltd.) filled with dry Ar gas (H_2O < 1 ppm and O_2 < 1ppm). Red P powder (Wako Pure Chemical Industries, purity 98%) and AB powder (Wako Pure Chemical Industries) were used as-purchased. The P and AB powders were loaded in a ball-milling vial coated by zirconia in the 6:4 w/w ratio and ball-milled at 900 rpm for 3 h (ball : powder ratio = 35:1 w/w) under Ar atmosphere. The negative electrode was prepared by mixing the obtained material (P/AB), AB conductive additive (the same material used to prepare the P/AB composite), and polyamideimide (PAI) binder in 75 : 15 : 10 wt% in *N*-methyl-2-pyrrolidone (Wako Pure Chemical Industries, Japan, purity 99%) using a planetary mixer (AR-100, Thinky). The resulting slurry was coated on a Cu foil and dried at 60 °C in a vacuum oven for 10 h. 10 mm diameter disks were then punched out and dried at 120 °C under vacuum overnight. Commercial $LiFePO_4$ powder (Tatung Fine Chemical Co, Taiwan) with a carbon content of ~2 wt% was used as a positive electrode for full-cell investigations. The positive electrode was prepared using the same procedures as the negative electrode, but with the composition of 85 : 10 : 5 wt% ($LiFePO_4$: AB: PAI). The typical mass loadings of the P/AB and $LiFePO_4$ active materials were 0.75 mg cm^{-2} (P loading ~0.45 mg cm^{-2}) and 8.65 mg cm^{-2}, respectively, and a capacity ratio of 1.15 (positive/negative) was selected based on practical capacities obtained from the half-cells, based on the irreversible capacity in the first cycle. The salts, Li[FSA] (Kishida Chemical, water content < 20 ppm, purity > 99%) and $[C_2C_1im][FSA]$ (Kanto Chemical, water content < 30 ppm, purity > 99%), were dried in a vacuum line overnight

at 80 °C. The IL electrolyte was prepared by mixing Li[FSA] and $[C_2C_1im][FSA]$ in the 2:8 and 5:5 mol ratios, hereafter denoted as $IL_{2:8}$ and $IL_{5:5}$, respectively, and dried again in a vacuum line at 80 °C. The organic electrolytes, 1 mol dm^{-3} $Li[PF_6]$-EC/DMC (1:1 v/v; Kishida Chemical Co. Ltd.,) (Org_{PF6}), 1 mol dm^{-3} Li[FSA]-EC/DMC (1:1 v/v) (Org_{FSA}), and Li[FSA]-EC/DMC (1:1 v/v) with 3 wt% fluoroethylene carbonate (FEC) (Sigma Aldrich, purity 99%) (Org_{FEC}), were used as control electrolytes. The Org_{FEC} was prepared by adding 3 wt% FEC to Org_{FSA}.

2.2 Characterizations

The P/AB powder was characterized by XRD and Raman spectroscopy. The XRD patterns were obtained using a Rigaku SmartLab diffractometer (Cu Kα (λ = 1.5418 Å) and 40 kV−30 mA) equipped with a Si strip high-speed detector (D-teX Ultra 250, Rigaku) under a Bragg-Brentano geometry at the scan rate of 0.5 deg min^{-1}. The Raman spectra were obtained using a DXR3 Smart Raman (Thermo Fisher Scientific) equipped with a 532 nm diode-pumped solid-state laser at the resolution of 2 cm^{-1}. The particle size measurement and morphology observation were performed by SEM (Hitachi, SU-8020) and the elemental composition was evaluated by EDX (Horiba EMAXEvolution X-max). The XPS analysis of the P/AB pristine powder was carried out using a JEOL JPS-9010 XPS instrument (MgKα (λ = 9.89 Å), 10 kV−10 mA) with Ar etching at the ion energy of 400 eV for 5 and 10 s. The obtained spectra were analyzed using analytical software (SpecSurf, ver. 1.8.3.7, JEOL, Ltd).

2.3 Electrochemical analysis

2.3.1 Two-electrodes cell

A 2032-type coin cell was assembled with the test electrode and Li metal (Sigma–Aldrich, > 99.9% purity) counter electrode on a stainless steel plate. A glass fiber filter (Whatman, GF-A, 260 mm in thickness and 16 mm in diameter) soaked with the electrolyte was used as a separator. The charge-discharge, rate capability, and cycleability tests were performed using an HJ1001SD8 charge−discharge test device (Hokuto Denko, Japan). The charge-discharge tests were conducted at current rates of 250 mA g^{-1} and 16 mA g^{-1} in the cut-off voltage range of 0.005–2.0 V and 1.6–3.8 V for half-cell and full-cell, respectively. The operating temperature was maintained at 25 °C using ESPEC SU221 thermostatic chamber. Electrochemical impedance spectroscopic tests were conducted with cycling at current densities of 250 mA g^{-1} (half-cell) and 16 mA g^{-1} (full-cell) for 1-3 cycles and 500 mA g^{-1} (half-cell) and 32 mA g^{-1} (full-cell) for 4-10 cycles, respectively. The impedance spectra were measured at 0.5 V and 2.7 V in half-cell and full-cell, respectively, during the charging step at the 2nd, 4th, and 11th cycles in the frequency range of 100 kHz–10 mHz and voltage amplitude of 20 mV.

2.3.2 Three-electrode cell

To understand the charge-discharge behavior of negative and positive electrodes in the full-cell configuration, a disk-type three-electrode cell (SB7, EC Frontier) was employed. The ratio of mass loading between positive and negative electrodes was set according to the capacities obtained in the P/AB half-cell tests and accounting for Li loss in the irreversible capacity during the first cycle. The current density of 16 mA g^{-1} was calculated based on the weight of the $LiFePO_4$ positive electrode. Based on the results obtained in the full-cell tests in the coin cell, the cut-off voltage range of the three-electrode cell was maintained at 1.6–3.8 V. However, the cut-off voltage of the

positive and negative electrodes relative to the Li metal reference electrode was kept wider than that in half-cells to ensure that the full-cell operation limits the capacities of charging and discharging. The gravimetric energy density of the full cell was calculated based on the following formula:

$$W = V_{\text{avg}} \times \frac{C_{\text{LiFePO4}} \times C_{\text{P-AB}}}{C_{\text{LiFePO4}} + C_{\text{P-AB}}}$$

where W is the gravimetric energy density, V_{avg} is the average voltage of operation calculated by dividing the area under the discharge curve of voltage vs. capacity of the full-cell, C_{LiFePO4} and $C_{\text{P-AB}}$ are the obtained gravimetric capacities of $LiFePO_4$ and P/AB in the three-electrode cell.

2.3.3 Ex-situ electrode analysis

The charge-discharge mechanism was investigated using ex-situ XRD and XPS analysis after charging and discharging the P/AB electrodes to the prescribed charged and discharged states. The electrodes were taken out by disassembling the coin cells followed by washing with tetrahydrofuran (THF) and subsequently drying under vacuum overnight. The evolution of morphology and composition of the SEI layer with cycling in different electrolytes were investigated by SEM and XPS. Argon ion etching at an energy of 400 eV was performed for 20 s in the interval of 5 s to obtain the depth profile of the electrodes.

3. Results and discussion

The P/AB (6:4 w/w) composite powder was prepared through a one-step high energy ball-milling at a milling speed of 900 rpm. For preliminary characterization, XRD patterns were derived from P/AB alongside the precursor materials red P and AB, as shown in Figure 1a. The XRD

patterns reveal P/AB to be a low crystalline material with no characteristic peaks, whereas some broad peaks are observed in red P and AB powders, in congruence with previous reports.[49-50] The amorphization of the product can be attributed to the continuous fracturing and impact induced by the intense ball-milling conditions on the precursor materials. A decrease in the crystallite size of the graphene sheets is confirmed by a subsequent Raman spectrum obtained from P/AB at an I_D/I_G ratio of 1.45(Figure 1b), which displays two distinct peaks corresponding to the D (~1350 cm^{-1}) and G (~1590 cm^{-1}) bands of carbon materials.

For further scrutiny, SEM, TEM, EDX, and XPS analyses were conducted on the P/AB composite powder. As illustrated by the SEM images (Figure 1c), the P/AB particle sizes were found to fall in the 1–10μm range. EDX mapping (Figure 1d) displayed a consistent contrast throughout the particle, depicting a uniform distribution of the P and C elements. Further, the amount of resident P and C elements were determined to be 59.3 wt% and 37.7 wt%, respectively (relatively close to the initial amounts (6:4 w/w) used for preparation), as shown in Figure S1. A small amount of O (3.0 wt%), attributed to native O on the P and AB precursor material or O contamination during the ball-milling procedure, is also found in the P/AB particle.

The bonding states of the elements at different depths of P/AB were derived from XPS spectra obtained at different Ar etching times (0s, 5s, and 10s) as shown in Figure 1e (P 2p), Figure 1f (C 1s), and Figure 1g (O 1s). At 0s, in the P 2p spectrum, two distinct peaks which are further deconvoluted into four peaks corresponding to the P-P bond ($2P_{3/2}$: 129.7 eV and $2P_{1/2}$: 130.5 eV) and P-O bond ($2P_{3/2}$: 133.4 and $2P_{1/2}$: 134.2 eV) were observed.[51-52] After 5s of Ar bombardment, the P-O bond peak significantly fades, leaving the P-P bond peak to dominate the spectrum. No significant changes were observed after etching is prolonged to 10s. In the C 1s spectrum, a peak assignable to the C-O bond is observed at 0s. However, the peak is seen to shift to the lower binding

energy of 284.6 eV after 5s of etching, denoting the presence of a C-C bond [53]. In the O 1s spectrum, a broad peak deconvoluted to P-O bond (533 eV) and C-O bond (532 eV) can be observed at 0s etching time. After continued etching for 5s and 10s, the peak intensity diminished, corroborating the P 2p and C 1s spectra results.

To understand the electrochemical performance of P/AB in both organic and ionic liquid electrolytes, galvanostatic charge-discharge tests were performed on Li|P/AB half-cells with (a) Org_{PF6}, (b) Org_{FSA}, (c) Org_{FEC}, (d) $IL_{2:8}$, and (e) $IL_{5:5}$ electrolytes. Charge-discharge curves were obtained for the 1st, 2nd, 10th and 50th cycles, as shown in Figure 2. In the first cycle, high discharge capacities of 1536 mAh $(g\text{-}P/AB)^{-1}$ for Org_{PF6}, 1598 mAh $(g\text{-}P/AB)^{-1}$ for Org_{FSA}, 1386 mAh $(g\text{-}P/AB)^{-1}$ for Org_{FEC}, 1600 mAh $(g\text{-}P/AB)^{-1}$ for $IL_{2:8}$, and 1431 mAh $(g\text{-}P/AB)^{-1}$ for $IL_{5:5}$ were achieved along with Coulombic efficiencies of 87.6%, 88.2%, 85.3%, 88.0%, and 86.7 %, respectively. Although all electrolytes display high reversibility in the second cycle, a significant increase in polarization is observed in Org_{PF6} and Org_{FSA} after 50 cycles. On the other hand, only a small increase in polarization during discharge is noted in Org_{FEC}, $IL_{2:8,}$ and $IL_{5:5}$ throughout the cycling process.

For a clear picture of the redox process during the half-cell operations, d*Q*/d*V* plots derived from the charge-discharge curves and cyclic voltammograms are shown in Figures S2 and S3, respectively. During the charging process of the first cycle, two peaks are noted in each of the electrolytes. The small peak appearing in the high voltage region represents the start of electrolyte decomposition, whereas the large peak in the low voltage region corresponds to the commencement of the lithiation process of P. As illustrated by Figure S2(a-e), electrolyte decomposition is seen to start at 1.35 V (Org_{PF6}), 1.41 V (Org_{FSA}), 1.44 V (Org_{FEC}), 1.45 V ($IL_{2:8}$), and 1.45 V ($IL_{5:5}$), demonstrating that the decomposition of Org_{FEC} and IL electrolytes occurs at

higher voltages than in Org_{PF6} and Org_{FSA}. Similar findings were reported by a study on an organic electrolyte (1 mol dm^{-3} $LiPF_6$ in EC) with FEC additive (10 wt%), which suggested that FEC in a solvated complex is preferentially reduced to passivate the negative electrode surface.[54] The results also indicate redox potentials of ~0.7 and 0.92 V vs. Li^+/Li in the charging (lithiation) and discharge (delithiation) processes, respectively, for all the electrolytes. However, redox activity in Org_{PF6} and Org_{FSA} is noted to diminish significantly after 50 cycles. In contrast, redox activity in Org_{FEC} and the IL electrolytes was maintained albeit with a slight increase in polarization, indicative that the electrolyte plays a vital role in improving the reversibility of the P/AB electrode. The cyclic voltammograms strongly supported the results obtained from the d*Q*/d*V* plots, because overlapping of anodic peaks is clearly observed in the 2nd and 3rd cycles in $IL_{2:8}$ and $IL_{5:5}$ (Figure S3 (d) and (e)), indicating the enhanced reversibility in IL electrolytes compared to the decreasing current in Org_{PF6} and Org_{FSA} (Figure S3 (a) and (b)).

In order to eliminate the influence of the Li metal counter electrode on the performance of the P/AB electrode, charge-discharge curves for the first two cycles were obtained from P/AB|$LiFePO_4$ full cells comprising the above-mentioned (a) Org_{PF6}, (b) Org_{FSA}, (c) Org_{FEC}, (d) $IL_{2:8}$, and (e) $IL_{5:5}$ electrolytes in the voltage range of 1.6–3.8 V at the current rate of 16 mA $(g\text{-}LiFePO_4)^{-1}$ as shown in Figure 3. The capacity was calculated based on the weight of $LiFePO_4$. The weight ratio of $LiFePO_4$ to P/AB was adjusted to 11.5 in weight (positive/negative capacity ratio = 1.15) based on reversible discharge capacities obtained from the half-cell configurations and compensation of the irreversible capacity. Org_{PF6} and Org_{FSA} yielded discharge capacities of 125 and 128 mAh g^{-1} with Coulombic efficiencies of 81.4 and 79.9 % in each case, as shown in Figures 3(a, b). The capacity decreased to 104 and 120 mAh g^{-1} in the second cycle with an increase in polarization, conforming to the half-cell test results (Figure 2(a-b)). In Org_{FEC}, $IL_{2:8}$,

and $IL_{5:5}$, comparable first discharge capacities of 124 mAh g^{-1}, 125 mAh g^{-1} and 122 mAh g^{-1} along with Coulombic efficiencies of 80.8%, 83.2% and 82.8 % were achieved (Figures 3(c-e)). The first and second cycle discharge curves appear to overlap, indicating improved reversibility in FEC-added and IL electrolytes. For facile comparison of increase in polarization with cycling in different electrolytes, the charge-discharge curves of the 1st and 50th cycles in both half-cell and full-cell configurations are plotted in Figure S4 (a) and (b), respectively.

To ascertain other electrochemical parameters of the P/AB electrode in the aforementioned electrolytes, the P/AB|$LiFePO_4$ full cells were subjected to cycle tests, rate capability tests, and EIS tests, as displayed in Figure 4. The $IL_{2:8}$ electrolyte achieves the highest capacity retention of 75.0 % (78 mAh g-$(LiFePO_4)^{-1}$) after 200 cycles at a current density of 80 mA g^{-1}, as can be seen in Figure 4a. $IL_{5:5}$ and Org_{FEC} electrolytes yielded lower capacity retention of 62.5% and 59.0 %, respectively. Additionally, high Coulombic efficiencies of 99.9% ($IL_{2:8}$), 99.8% ($IL_{5:5}$), and 99.7 % (Org_{FEC}) are also achieved at the 200th cycle. In the case of Org_{PF6} and Org_{FSA}, immense capacity fading is observed during the first 50 cycles. As such, rate capability was tested for the three electrolytes (Org_{FEC}, $IL_{2:8}$ and $IL_{5:5}$) in the current density range of 16−80 mA g-$(LiFePO_4)^{-1}$ as illustrated by Figure 4b. At 80 mA g-$(LiFePO_4)^{-1}$, both $IL_{2:8}$ and $IL_{5:5}$ demonstrate a high rate performance of 92 and 91 mAh g^{-1} each, whilst Org_{FEC} attains 82 mAh g^{-1}.

To observe the effect of FEC additive in a PF_6^- based organic electrolyte, the electrochemical performance of Li|P/AB half cells and P/AB|$LiFePO_4$ full cells were investigated using 1 M Li[PF_6] in EC:DMC with 3 wt% FEC electrolyte (Org_{PF6} with FEC additive), and the resulting data is shown in Figure S5. A discharge capacity of 1472 mAh g^{-1} was observed for a Li|P/AB half cell in the 1st cycle with a Coulombic efficiency of 85.4%. The P/AB|$LiFePO_4$ full cell provides the 1st cycle discharge capacity of 123.6 mAh g^{-1} with a Coulombic efficiency of

80.3%. The capacity retentions were 23.9 % and 22.1 % for the half-cell and full-cell, respectively, after 50 cycles which is similar to Org_{PF6} (without FEC additive) as shown in Figure S6 (a). It should be noted that the Coulombic efficiency in Org_{PF6} during cycling is consistently lower than 100 % in full-cell configuration, whereas, it exceeded 100% in half-cell configuration (Figure S6) suggesting possible effects of the reduced species from the Li metal counter electrode. From the evaluation of electrochemical performance of the half cells and full cells using the series of organic and IL electrolytes, there is an insignificant effect of the Li salt content in the IL electrolytes and FEC additive in the organic electrolyte. Hence, further characterization was done with $IL_{2:2}$ and Org_{PF6} without FEC additive.

For insight into the influence of the SEI layer on the P/AB electrode performance, Nyquist plots of the 1st, 3rd and 10th cycles of P/AB|$LiFePO_4$ full cells utilizing Org_{PF6}, Org_{FSA}, Org_{FEC}, and $IL_{2:8}$ electrolytes were obtained as shown in Figure 4 (c-f). The organic electrolytes demonstrate large interfacial resistances with continued cycling in contrast with $IL_{2:8}$, whose interfacial resistance is lower by one order of magnitude and remains constant with continued cycling, evincing the formation of a more robust SEI layer in IL electrolytes. The results are further corroborated by similar electrochemical performance tests (cycle tests, rate capabilities, and EIS Nyquist plots) performed on Li|P/AB half-cells utilizing the above-mentioned electrolytes as seen in Figure S6 (c-f). Similarly, the P/AB electrode in $IL_{2:8}$ displays the best electrochemical performance and lower interfacial resistance, which can be ascribed to the contribution of IL electrolytes.

The P/AB electrode showed high capacity and stable cycleability with the IL electrolyte. Although high-capacity negative electrode materials are extremely crucial to high-energy density LIBs, it is equally important to elucidate the individual contribution of positive and negative

electrodes in the battery. Thus, a three-electrode cell was employed to ascertain the performance of the individual electrodes and calculate the energy density of the P/AB|$LiFePO_4$ full-cell utilizing the $IL_{2:8}$ electrolyte. The resulting galvanostatic charge-discharge curves from the first cycle are shown in Figure S7 (energy density was calculated based on the formula given in the Experimental section). The obtained values of V_{avg}, $C_{LiFePO4,}$ and $C_{P\text{-}AB}$ are 2.38 V, 120 mAh $(g\text{-}LiFePO_4)^{-1}$, and 1400 mAh $(g\text{-}P/AB)^{-1}$, respectively, accomplishing an energy density (W) of 263 Wh $(kg\text{-}(LiFePO_4 + P/AB))^{-1}$. The resulting value falls in the high end of the energy density range available in current LIBs.

To further scrutinize the evolution of the SEI layer components electrode with continued cycling, XPS depth profiling was conducted on the P/AB electrode upon Ar etching for 5s, 10s and 20 s after the 1st and 50th cycle in the Org_{PF6}, Org_{FSA}, Org_{FEC}, and $IL_{2:8}$ electrolyte systems as illustrated by the XPS spectra in Figures 5 and S8 (see Table S2 for binding energies of the species). A key difference in the SEI composition between the electrodes in Org_{FSA}, Org_{FEC}, and $IL_{2:8}$ electrolytes emerges in the S 2p spectra after the 1st cycle, as shown in Figure 5(a-c). For electrodes in Org_{FSA} and Org_{FEC}, a large peak attributed to FSO_2– appears at a high binding energy (171.5 eV).[55] However, after 5s of etching, only a negligible amount of sulfur can be detected. Continued etching results in a further decrease in intensity, suggesting that the sulfur species are only present on the surface of the P/AB electrode in Org_{FSA} and Org_{FEC}. Conversely, for the P/AB electrode in $IL_{2:8}$, sulfur species are detected even at deeper levels of the SEI layer. Although a broad peak consisting of FSO_2– and SO_4^{2-} (169.4 eV)[56] species was observed even before Ar bombardment, the FSO_2– component almost disappears after 5s of etching. When etching is prolonged to 10s, S^{2-} species emerge at 162.4 eV[57] and continue to dominate the SEI layer even after 20s of etching. This suggests that the $IL_{2:8}$ electrolyte facilitates the formation of multiple layers of sulfur-based

components in the SEI. In a previous study on NIBs utilizing hard carbon electrodes alongside Na[FSA]-[C_3C_1pyrr][FSA] IL electrolytes, sulfur-based components in an SEI layer were reported to be beneficial to electrochemical performance.[58] On this account, the improved cycleability and high rate performance noted in the $IL_{2:8}$ electrolyte could also be ascribed to the presence of sulfur-based components in the SEI layer.

To shed light on the electrolyte decomposition behavior during cycling, it is imperative to elucidate the cation and anion coordination environment in the electrolytes. Thus, Raman spectra of the Org_{FSA}, Org_{FEC}, and $IL_{2:8}$ electrolytes were obtained, as shown in Figure S9 (see Supporting Information for a detailed discussion). In Org_{FSA} and Org_{FEC}, each Li^+ is coordinated with four EC solvent molecules, whereas Li^+ is coordinated with the FSA^- anion in $IL_{2:8}$. This coordination decreases the energy of lower unoccupied molecular orbital, promoting the reductive decomposition of these coordinated species resulting in different properties of SEI layers in organic and IL electrolytes, as also observed in XPS result (Figure 5 and Figure S8).

To understand the electrode morphology in respect to cycling, SEM images of the P/AB electrodes were obtained after the 1st cycle and the 50th cycle in Org_{PF6}, Org_{FSA}, Org_{FEC} and $IL_{2:8}$ as shown in Figure 6 (a-h). For the electrodes in the organic electrolytes, significant changes characterized by immense volume expansion and massive crack development after 50 cycles were observed (Figure 6 (a, b), (c, d), and (e, f)). A schematic diagram derived from the XPS and SEM analyses is provided in Figure 6i to illustrate the surface evolution during cycling in the different electrolyte systems. In the organic electrolytes (Org_{PF6}, Org_{FSA} and Org_{FEC}), the SEI layer formed on the P/AB electrode after the first cycle consists of LiF (product of PF_6^-, FSA^- anion, or FEC additive decomposition) and Li_2O and Li_2CO_3 (product of EC or DMC solvent decomposition). After 50 cycles, the substantial changes in volume and cracks on the particle surfaces suggest the

formation of fragile and unstable SEI layers that fail to suppress the pulverization of the active material and subsequent capacity fading. However, for the electrode in the $IL_{2:8}$ electrolyte, a crack-free surface with no distinguishable changes in particle morphology is seen even after 50 cycles (Figure 6 (g, h)). As illustrated by the schematic in Figure 6j, the SEI layer formed by $IL_{2:8}$ is uniform and robust, consisting primarily of sulfur species such as FSO_2^-, SO_4^{2-} and S^{2-} (a decomposition product of FSA^- anion) that protect the electrode from interparticle contact and thus facilitate high cycleability.

To explicate the charge-discharge mechanism of the P/AB negative electrode in $IL_{2:8}$, ex-situ XPS and XRD were performed on the P/AB electrode at different stages of the charge-discharge of the first cycle, as highlighted in Figure 7. The inset on the top right illustrates the measurement points in the charge-discharge curve ((1) pristine state, charging states ((2) 0.75 V, (3) 0.5 V, and (4) 0.005 V) and discharging states ((5) 0.92 V and (6) 2.0 V)). As shown in the ex-situ P 2p XPS of the electrode in Figure 7a, the spectrum before charging is the same as that of the pristine powder (Figure 1e) before etching. In its pristine state (Figure 7a (spectrum 1)), the spectrum is composed of P−O and P−P bond peaks. The P 2p spectra shown in Figure 7a (2-6) were obtained after 60-second Ar etching to strip off the SEI layer. During the charging process from 0.75 V to 0.005 V, the P-P bond intensity steadily decreases while another broad peak concurrently emerges at a low binding energy. The new broad peak can be deconvoluted into four main peaks at 128.2 eV ($2p_{3/2}$), 129.2 eV ($2p_{1/2}$) and 126.5 eV ($2p_{3/2}$), 127.3 eV ($2p_{1/2}$) assigned to LiP and Li_3P [59] in the full charging state at 0.005 V (Spectrum (4)). When the P/AB electrode is subjected to prolonged Ar etching for 2, 5 and 10 minutes at a fully charged state (Figure S10), the intensity of the Li_3P peaks becomes stronger, indicating the formation of Li_3P deeper into the core of the particle as reported in previous literature.[59] The deconvoluted peaks at 133.3 eV ($2p_{3/2}$) and 134.3 eV ($2p_{1/2}$)

corresponding to P−O bonds remain unperturbed by charging and discharging. After discharging (Spectra (5) and (6)), the peaks of LiP and Li_3P are noted to gradually diminish as the intensity of P-P peaks increases with continued discharging. For further investigation, ex-situ XRD was measured at full charged (4) and full discharge (6) states (Figure 7b). However, no peaks are observed in any case, suggesting that amorphous LiP and Li_3P are formed after charging. The results thus confirm successful lithiation and delithiation achieved during charging and discharging of the P/AB electrode in the IL electrolyte.

4. Conclusion

In this study, we investigate the influence of electrolytes (organic and IL electrolytes) on the charge-discharge behavior of the P/AB (6:4 w/w) negative electrode for LIBs using half-cell and full-cell configurations. On XRD, the P/AB composite prepared by high energy ball-milling was found to be an amorphous material, with 1–10μm sized particles of uniformly distributed P and C elements as confirmed by SEM and EDX. Although the resulting electrode achieved a high initial discharge capacity in the range of 1386–1700 mAh $(g\text{-}P/AB)^{-1}$ irrespective of the electrolyte used, the IL electrolyte exhibited significantly better rate and cycling performance compared to the organic electrolytes. A full cell utilizing a $LiFePO_4$ positive electrode and $IL_{2:8}$ electrolyte demonstrated stable charge-discharge behavior over 200 cycles with an average Coulombic efficiency of 99.9%. EIS tests conducted with cycling showed a significantly lower interfacial resistance in $IL_{2:8}$ compared to organic electrolytes. Electrode surface analysis through XPS analysis with Ar etching revealed an SEI layer consisting of multiple layers of sulfur species in the IL electrolytes, whereas in organic electrolytes, the SEI layers contained low sulfur content. Further, SEM employed to analyze the surface morphology of the P/AB electrode after cycling

established that the IL electrolyte suppressed massive volume changes, which resulted in good cycle performance. An energy density of 263 Wh (kg-($LiFePO_4$ + P/AB))$^{-1}$ was achieved using $IL_{2:8}$, evincing that the present P/AB electrode combined with an appropriate electrolyte is an auspicious candidate for cost-effective and high-energy density applications. Future work on this subject will focus on the optimization of full-cell parameters such as the weight ratio of positive and negative electrodes and the investigation of an optimized temperature range.

Acknowledgements

This work was supported by JSPS KAKENHI Grant Number 19H02811.

ASSOCIATED CONTENT

Supporting Information (PDF)

Supporting Information is available free of charge on the ACS Publications website at DOI: XXXXXXX.

Electrochemical data and EDX, XPS, and Raman spectroscopic data.

AUTHOR INFORMATION

Corresponding Author

E-mail: k-matsumoto@energy.kyoto-u.ac.jp (K.M.).

Notes

The authors declare no competing financial interest.

ORCID

Kazuhiko Matsumoto: 0000-0002-0770-9210

Rika Hagiwara: 0000-0002-7234-3980

Tables and Figures

Table 1. Summary of preparation methods for selected phosphorus-carbon composites and their electrochemical performance as negative electrode materials in different electrolytes for LIBs.

Negative electrode material	Preparation method	Electrolyte	First cycle capacity/ Coulombic efficiency (mAh g^{-1}/%)	Cut-off voltage (V)	Capacity retention (mAh g^{-1}/n cycles)	Ref.
BP/Super P	Ball-milling	$LiPF_6$ in EC/DEC	1814/90	0.0–2.0 0.78–2.0	600/100	[20]
RP/SCNT	Hydrothermal self-assembly	$LiPF_6$ in EC/DMC	1600/77	0.01–3.0	782/3000	[21]
Ring shaped RP/MWCNT	Vapor phase reaction	$LiPF_6$ in EC/DEC	-	0.01–3.0	444/500	[22]
RP/rGO	Hydrothermal process	$LiPF_6$ in DEC/DMC/EMC	1600/-	0.001–2.5	1000/80	[28]
RP/graphene	Solution-based method	$LiPF_6$ in DEC/DMC/EMC	1555/72	0.01–3.0	1286/100	[29]
RP/graphite	Thermal vapor deposition	$LiPF_6$ in EC/DMC/ EMC	740/72	0.005–3.0	485/50	[60]
BP/graphite	Ball-milling	$LiPF_6$ in EC/DMC/ EMC	2382/85	0.01–2.5	80% after 100 cycles	[25]
BP/AB	Ball-milling	Li_2S–P_2S_5 (80:20 mol%)	1962/89	0.0–2.5	1350/30	[61]
RP/AB	Ball-milling	Li[FSA]-$[C_2C_1im][FSA]$ (2:8 mol)	1600/88	0.005–2.0	1146/350	This work

*The concentration of electrolytes was 1 mol dm^{-3} unless specified otherwise.
** BP = black phosphorus; RP = red phosphorus; SCNT = single-walled carbon nanotubes; MWCNT = multi-walled carbon nanotubes; rGO = reduced graphene oxide
*** EC = ethylene carbonate; DMC = dimethyl carbonate; DEC = diethyl carbonate; EMC = ethyl methyl carbonate

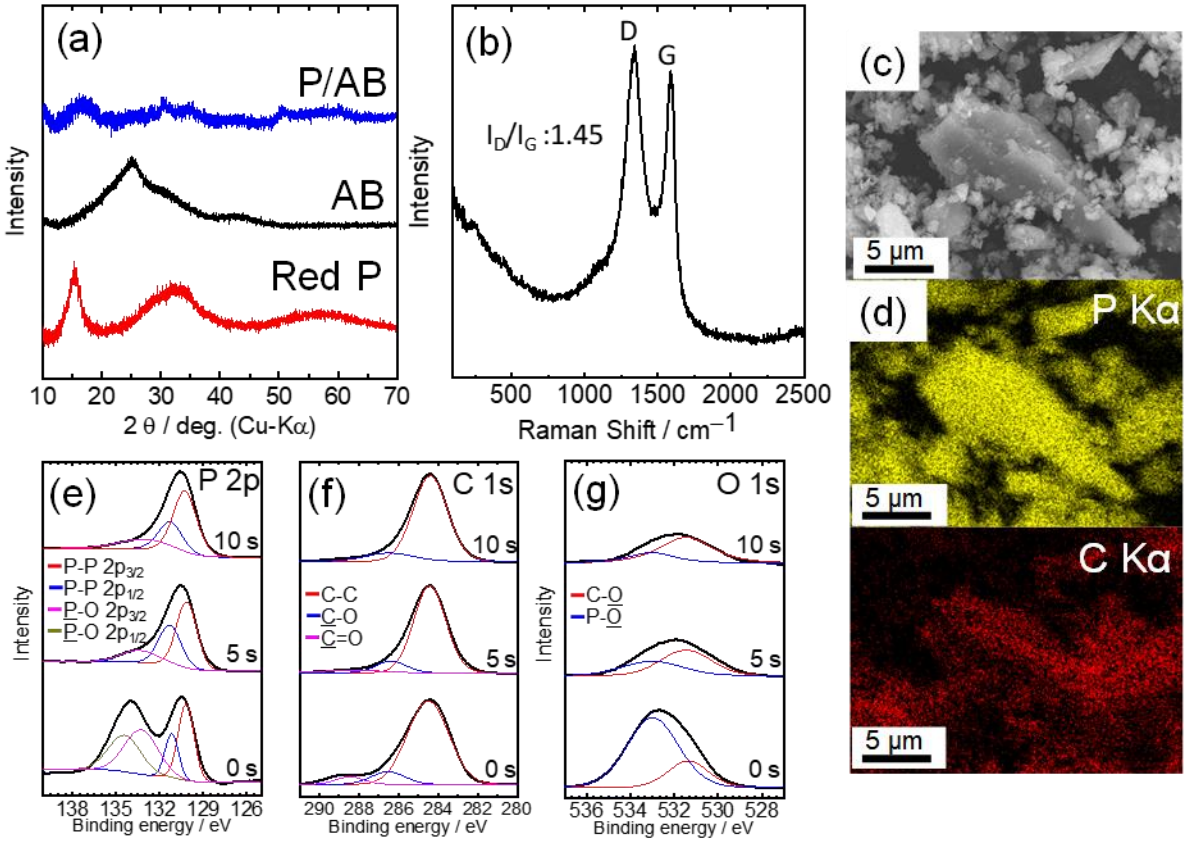

Figure 1. (a) XRD patterns of red P, AB, and P/AB powder. (b) Raman spectrum, (c) SEM image, and (d) EDX elemental mapping (P and C) of the P/AB powder. XPS with Ar etching (time = 0, 5 and 10 s) of the P/AB powder in (e) P 2p, (f) C 1s, and (g) O 1s regions. The P/AB powder was prepared by high-energy ball milling as shown in the Experimental section.

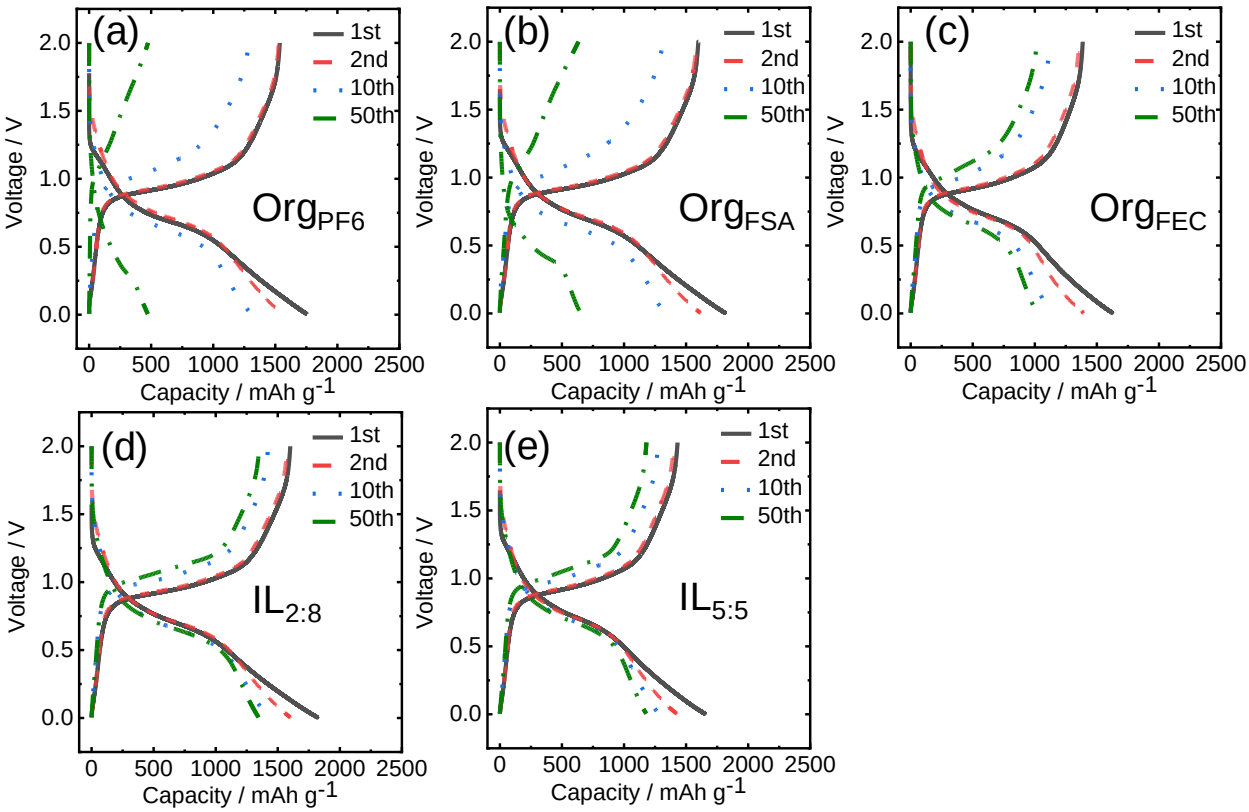

Figure 2. Galvanostatic charge-discharge curves of the Li|P/AB half cells (1st, 3rd, 10th, 50th cycle) using (a) Org_{PF6}, (b) Org_{FSA}, (c) Org_{FEC}, (d) $IL_{2:8}$, and (e) $IL_{5:5}$ electrolytes (current density = 250 mA g^{-1} (1-3 cycles) and 500 mA g^{-1} (4-50 cycles); cut-off voltage = 0.005–2.0 V). The capacity calculated takes into account the weight of the P/AB composite.

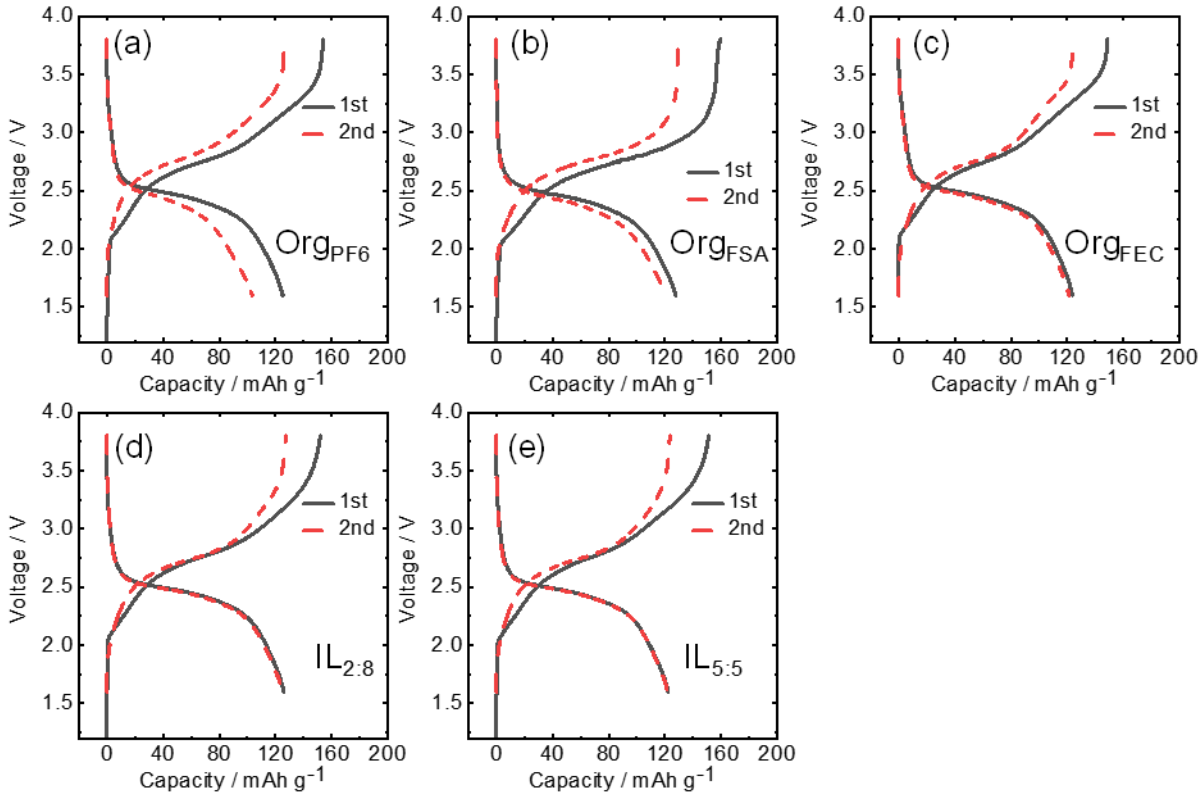

Figure 3. Galvanostatic charge-discharge curves of the P/AB|$LiFePO_4$ full cells (1st and 2nd cycles) using (a) Org_{PF6}, (b) Org_{FSA}, (c) Org_{FEC}, (d) $IL_{2:8}$, and (e) $IL_{5:5}$ electrolytes (current density = 16 mA g-$(LiFePO_4)^{-1}$; cut-off voltage = 1.6–3.8 V). The capacity calculated takes into account, the weight of $LiFePO_4$. The positive/negative capacity ratio is 1.15 (mass ratio: 11.5).

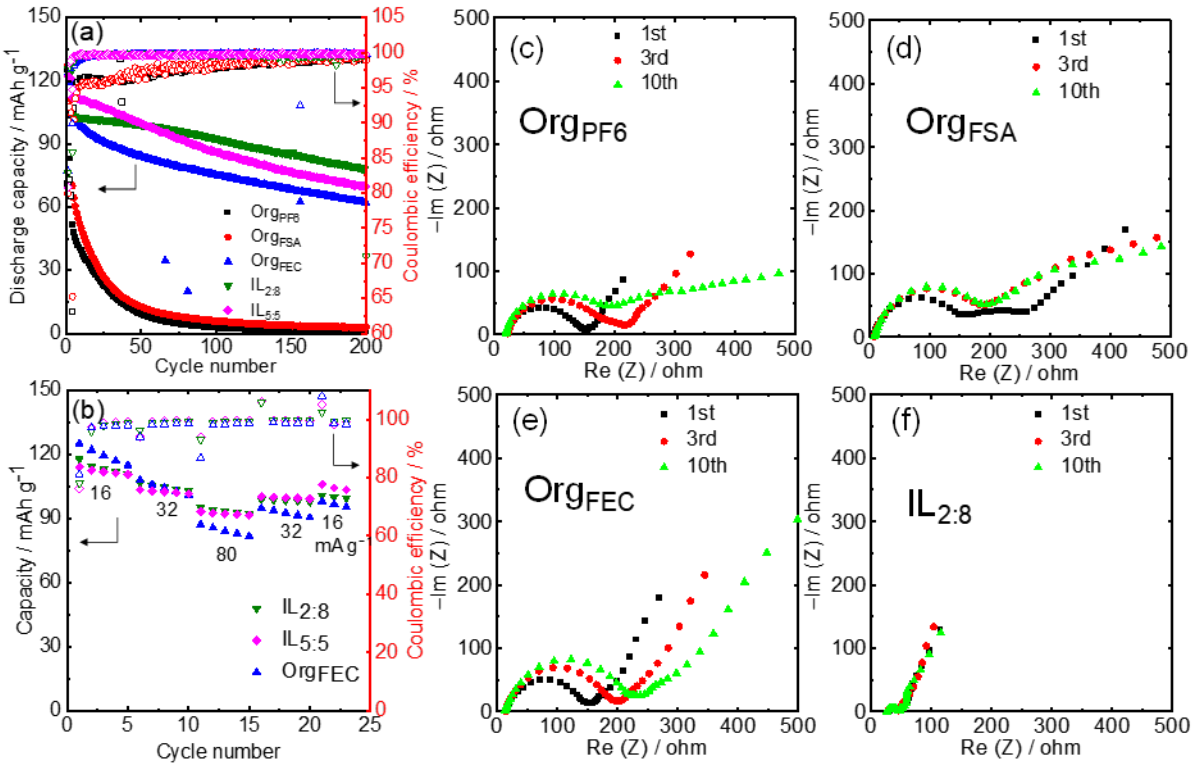

Figure 4. Electrochemical performance of the P/AB|$LiFePO_4$ full-cell and results of EIS tests at different cycles. (a) Cycle performance with Org_{PF6}, Org_{FSA}, Org_{FEC}, $IL_{2:8}$, and $IL_{5:5}$ electrolytes (Current density: 1-3 cycles = 16 mA $(g\text{-}LiFePO_4)^{-1}$, 4-200 cycles = 80 mA $(g\text{-}LiFePO_4)^{-1}$; cut-off voltage = 1.6–3.8 V). (b) Rate performance with Org_{FEC}, $IL_{2:8}$, and $IL_{5:5}$ (Current density: 16-80 mA $(g\text{-}LiFePO_4)^{-1}$; cut-off voltage = 1.6–3.8 V). Nyquist plots with (c) Org_{PF6}, (d) Org_{FSA}, (e) Org_{FEC}, and (f) $IL_{2:8}$ measured at 2.7 V in the charging steps of the 2nd, 4th, and 11th cycle.

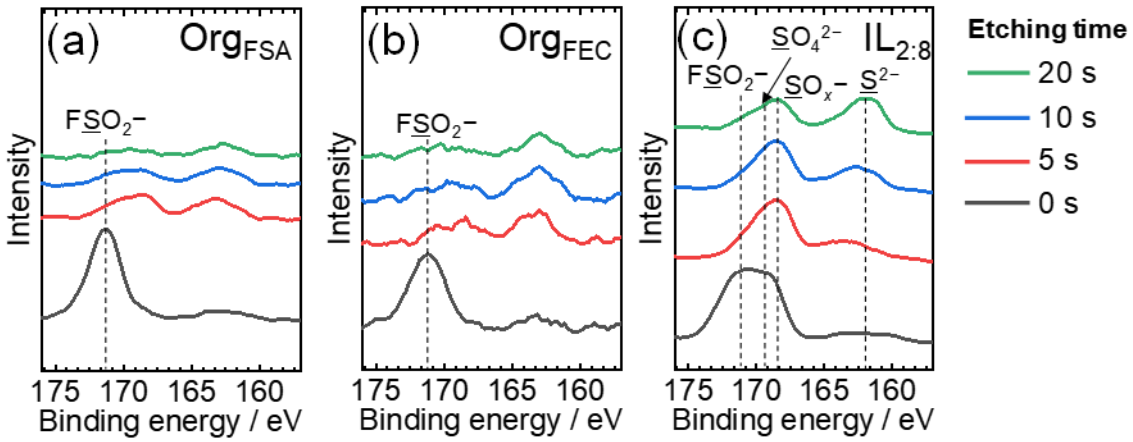

Figure 5. XPS spectra of the P/AB electrode with Ar etching after 1st cycle in S 2p regions, respectively using (a) Org_{FSA}, (b) Org_{FEC} and (c) $IL_{2:8}$ electrolytes.

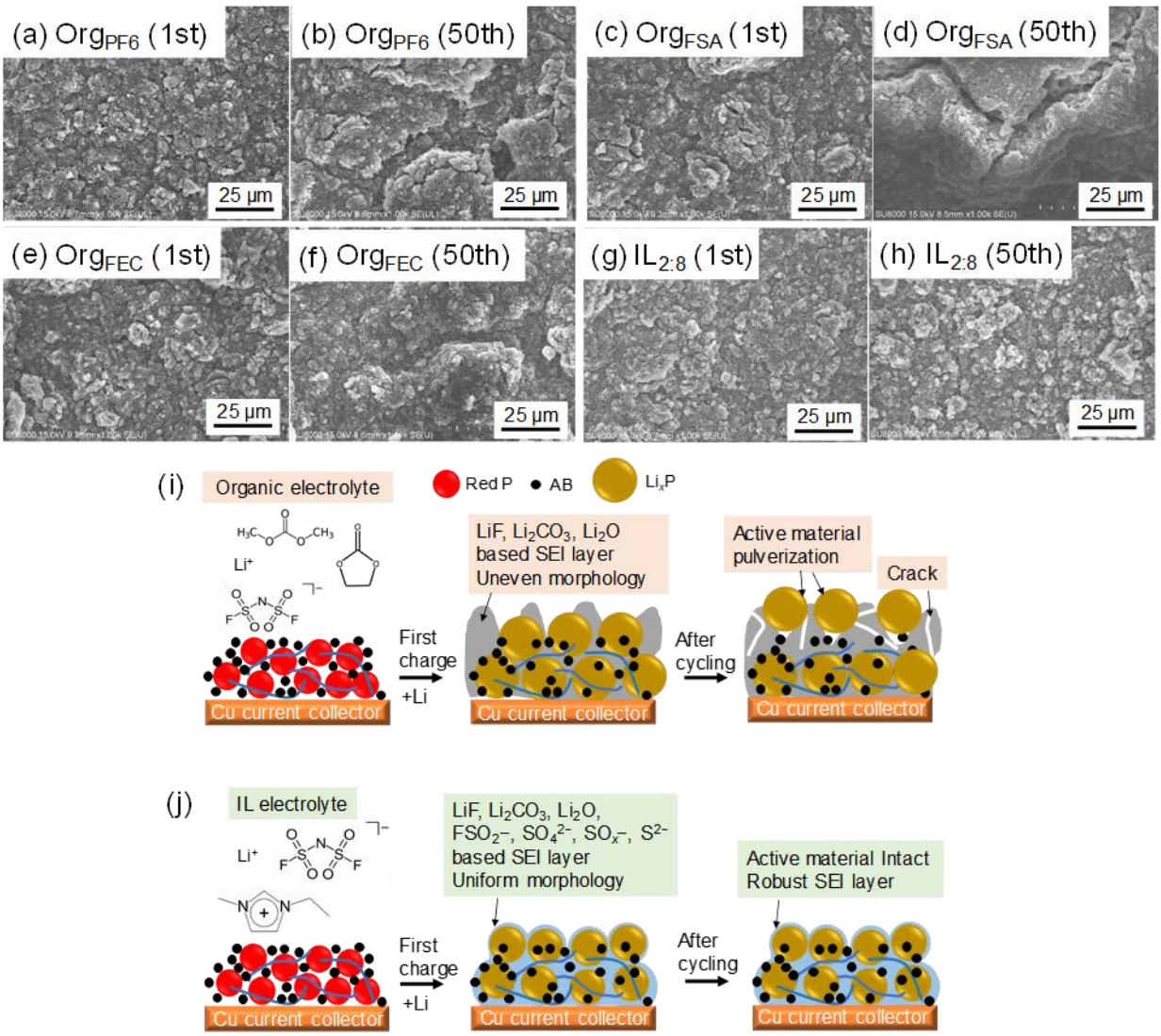

Figure 6. SEM images of the P/AB electrode after 1st and 50th cycles using (a, b) Org_{PF6}, (c, d) Org_{FSA}, (e, f) Org_{FEC}, (g, h) $IL_{2:8}$ electrolytes. Current density 250 mA g^{-1} (1-3 cycles) and 500 mA g^{-1} (4-50 cycles) and cut-off voltage = 0.005–2.0 V. Schematic comparison of the electrode surface evolution during cycling in (i) organic and (j) IL electrolytes.

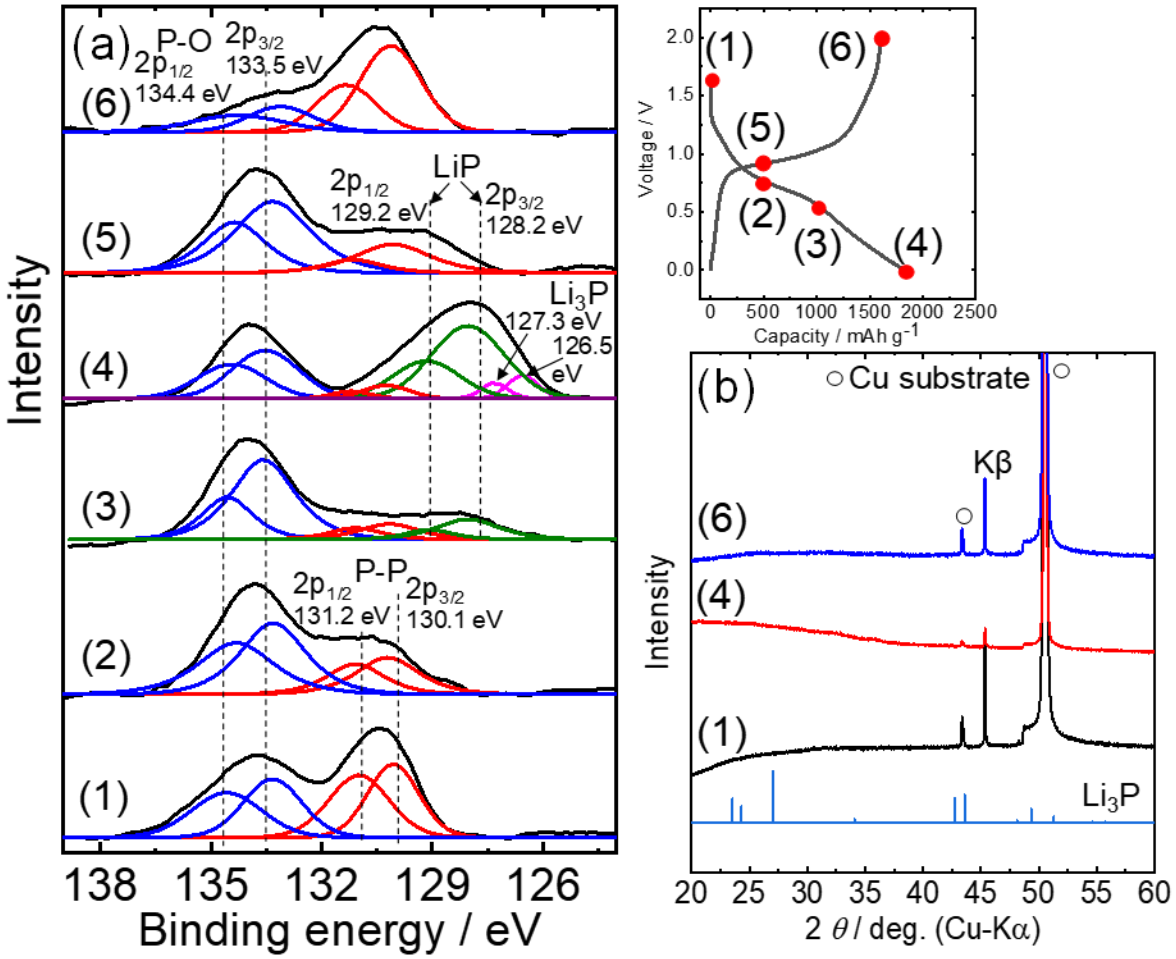

Figure 7. (a) The P 2p XPS of the P/AB electrode in the (1) pristine state, charging states ((2): 0.75 V, (3): 0.5 V, and (4): 0.005 V) and discharging states ((5): 0.92 V and (6): 2.0 V). (b) Ex-situ XRD patterns of the P/AB electrode in the (1) pristine state, (4) fully charged state (0.005 V), and (6) fully discharged state (2.0 V). The XPS spectra were taken after 60s Ar etching. Inset of the first cycle charge-discharge curve is provided to clarify the XPS and XRD measurement points.

References

1. Lu, L.; Han, X.; Li, J.; Hua, J.; Ouyang, M., A Review on the Key Issues for Lithium-Ion Battery Management in Electric Vehicles. *J. Power Sources* **2013,** *226*, 272-288.

2. Nitta, N.; Wu, F.; Lee, J. T.; Yushin, G., Li-Ion Battery Materials: Present and Future. *Mater. Today* **2015,** *18*, 252-264.

3. Endo, M.; Kim, C.; Nishimura, K.; Fujino, T.; Miyashita, K., Recent Development of Carbon Materials for Li Ion Batteries. *Carbon* **2000,** *38*, 183-197.

4. Aurbach, D.; Markovsky, B.; Shechter, A.; Ein‐Eli, Y.; Cohen, H., A Comparative Study of Synthetic Graphite and Li Electrodes in Electrolyte Solutions Based on Ethylene Carbonate‐Dimethyl Carbonate Mixtures. *J. Electrochem. Soc.* **1996,** *143*, 3809-3820.

5. Roberts, A. D.; Li, X.; Zhang, H., Porous Carbon Spheres and Monoliths: Morphology Control, Pore Size Tuning and Their Applications as Li-Ion Battery Anode Materials. *Chem. Soc. Rev.* **2014,** *43*, 4341-4356.

6. Bulusheva, L. G.; Okotrub, A. V.; Kurenya, A. G.; Zhang, H.; Zhang, H.; Chen, X.; Song, H., Electrochemical Properties of Nitrogen-Doped Carbon Nanotube Anode in Li-Ion Batteries. *Carbon* **2011,** *49*, 4013-4023.

7. Buiel, E.; Dahn, J. R., Li-Insertion in Hard Carbon Anode Materials for Li-Ion Batteries. *Electrochim. Acta* **1999,** *45*, 121-130.

8. Larcher, D.; Beattie, S.; Morcrette, M.; Edström, K.; Jumas, J.-C.; Tarascon, J.-M., Recent Findings and Prospects in the Field of Pure Metals as Negative Electrodes for Li-Ion Batteries. *J. Mater. Chem.* **2007,** *17*, 3759-3772.

9. Baggetto, L. c.; Notten, P. H. L., Lithium-Ion (De)Insertion Reaction of Germanium Thin-Film Electrodes: An Electrochemical and in Situ Xrd Study. *J. Electrochem. Soc.* **2009,** *156*, A169.

10. Nitta, N.; Yushin, G., High-Capacity Anode Materials for Lithium-Ion Batteries: Choice of Elements and Structures for Active Particles. *Part. Part. Syst. Charact.* **2014,** *31*, 317-336.

11. McDowell, M. T.; Lee, S. W.; Nix, W. D.; Cui, Y., 25th Anniversary Article: Understanding the Lithiation of Silicon and Other Alloying Anodes for Lithium-Ion Batteries. *Adv. Mater.* **2013,** *25*, 4966-4985.

12. Mukhopadhyay, A.; Sheldon, B. W., Deformation and Stress in Electrode Materials for Li-Ion Batteries. *Prog. Mater Sci.* **2014,** *63*, 58-116.

13. Huggins, R. A., Lithium Alloy Negative Electrodes. *J. Power Sources* **1999,** *81-82*, 13-19.

14. Liu, W.; Zhi, H.; Yu, X., Recent Progress in Phosphorus Based Anode Materials for Lithium/Sodium Ion Batteries. *Energy Storage Mater.* **2019,** *16*, 290-322.

15. Fu, Y.; Wei, Q.; Zhang, G.; Sun, S., Advanced Phosphorus-Based Materials for Lithium/Sodium-Ion Batteries: Recent Developments and Future Perspectives. *Adv. Energy Mater.* **2018,** *8*, 1703058.

16. Zhou, S.; Li, J.; Fu, L.; Zhu, J.; Yang, W.; Li, D.; Zhou, L., Black Phosphorus/Hollow Porous Carbon for High Rate Performance Lithium-Ion Battery. *ChemElectroChem* **2020,** *7*, 2184-2189.

17. Liu, H.; Zhang, S.; Zhu, Q.; Cao, B.; Zhang, P.; Sun, N.; Xu, B.; Wu, F.; Chen, R., Fluffy Carbon-Coated Red Phosphorus as a Highly Stable and High-Rate Anode for Lithium-Ion Batteries. *J. Mater. Chem. A* **2019,** *7*, 11205-11213.

18. Lin, W.; Huang, Y.-e.; Guan, L.; Huang, X.; Li, L.; Du, K.-Z.; Wu, X., Chalcogen-Doped Red Phosphorus Nanoparticles @ Porous Carbon as High-Rate and Ultrastable Anode for Lithium-Ion Batteries. *Carbon* **2020,** *170*, 85-92.

19. Liberale, F.; Fiore, M.; Ruffo, R.; Bernasconi, R.; Shiratori, S.; Magagnin, L., Red Phosphorus Decorated Electrospun Carbon Anodes for High Efficiency Lithium Ion Batteries. *Sci. Rep.* **2020,** *10*, 13233.

20. Park, C.-M.; Sohn, H.-J., Black Phosphorus and Its Composite for Lithium Rechargeable Batteries. *Adv. Mater.* **2007,** *19*, 2465-2468.

21. Yuan, T.; Ruan, J.; Peng, C.; Sun, H.; Pang, Y.; Yang, J.; Ma, Z.-F.; Zheng, S., 3d Red Phosphorus/Sheared Cnt Sponge for High Performance Lithium-Ion Battery Anodes. *Energy Storage Mater.* **2018,** *13*, 267-273.

22. Zhao, D.; Zhang, J.; Fu, C.; Huang, J.; Xiao, D.; Yuen, M. M. F.; Niu, C., Enhanced Cycling Stability of Ring-Shaped Phosphorus inside Multi-Walled Carbon Nanotubes as Anodes for Lithium-Ion Batteries. *J. Mater. Chem. A* **2018,** *6*, 2540-2548.

23. Zhang, Y.; Tao, H.; Li, J.; Yang, X., Achieving a High-Performance P/C Anode through P-O-C Bond for Sodium Ion Batteries. *Ionics* **2020,** *26*, 3377-3385.

24. Ramireddy, T.; Xing, T.; Rahman, M. M.; Chen, Y.; Dutercq, Q.; Gunzelmann, D.; Glushenkov, A. M., Phosphorus–Carbon Nanocomposite Anodes for Lithium-Ion and Sodium-Ion Batteries. *J. Mater. Chem. A* **2015,** *3*, 5572-5584.

25. Sun, J.; Zheng, G.; Lee, H.-W.; Liu, N.; Wang, H.; Yao, H.; Yang, W.; Cui, Y., Formation of Stable Phosphorus–Carbon Bond for Enhanced Performance in Black Phosphorus Nanoparticle–Graphite Composite Battery Anodes. *Nano Lett.* **2014,** *14*, 4573-4580.

26. Jiao, X.; Liu, Y.; Li, T.; Zhang, C.; Xu, X.; Kapitanova, O. O.; He, C.; Li, B.; Xiong, S.; Song, J., Crumpled Nitrogen-Doped Graphene-Wrapped Phosphorus Composite as a Promising Anode for Lithium-Ion Batteries. *ACS Appl. Mater. Interfaces* **2019,** *11*, 30858-30864.

27. Wang, L.; Guo, H.; Wang, W.; Teng, K.; Xu, Z.; Chen, C.; Li, C.; Yang, C.; Hu, C., Preparation of Sandwich-Like Phosphorus/Reduced Graphene Oxide Composites as Anode Materials for Lithium-Ion Batteries. *Electrochim. Acta* **2016,** *211*, 499-506.

28. Zhu, X.; Yuan, Z.; Wang, X.; Jiang, G.; Xiong, J.; Yuan, S., Hydrothermal Synthesis of Red Phosphorus @Reduced Graphene Oxide Nanohybrid with Enhanced Electrochemical Performance as Anode Material of Lithium-Ion Battery. *Appl. Surf. Sci.* **2018,** *433*, 125-132.

29. Sun, L.; Zhang, Y.; Zhang, D.; Zhang, Y., Amorphous Red Phosphorus Nanosheets Anchored on Graphene Layers as High Performance Anodes for Lithium Ion Batteries. *Nanoscale* **2017,** *9*, 18552-18560.

30. Xu, K., Electrolytes and Interphases in Li-Ion Batteries and Beyond. *Chem. Rev.* **2014,** *114*, 11503-11618.

31. Eshetu, G. G.; Grugeon, S.; Laruelle, S.; Boyanov, S.; Lecocq, A.; Bertrand, J.-P.; Marlair, G., In-Depth Safety-Focused Analysis of Solvents Used in Electrolytes for Large Scale Lithium Ion Batteries. *Phys. Chem. Chem. Phys.* **2013,** *15*, 9145-9155.

32. Ponrouch, A.; Monti, D.; Boschin, A.; Steen, B.; Johansson, P.; Palacín, M. R., Non-Aqueous Electrolytes for Sodium-Ion Batteries. *J. Mater. Chem. A* **2015,** *3*, 22-42.

33. Matsumoto, K.; Nishiwaki, E.; Hosokawa, T.; Tawa, S.; Nohira, T.; Hagiwara, R., Thermal, Physical, and Electrochemical Properties of Li[N(So2f)2]-[1-Ethyl-3-Methylimidazolium][N(So2f)2] Ionic Liquid Electrolytes for Li Secondary Batteries Operated at Room and Intermediate Temperatures. *J. Phys. Chem. C* **2017,** *121*, 9209-9219.

34. Galiński, M.; Lewandowski, A.; Stępniak, I., Ionic Liquids as Electrolytes. *Electrochim. Acta* **2006,** *51*, 5567-5580.

35. Osada, I.; de Vries, H.; Scrosati, B.; Passerini, S., Ionic-Liquid-Based Polymer Electrolytes for Battery Applications. *Angew. Chem. Int. Ed.* **2016,** *55*, 500-513.

36. MacFarlane, D. R.; Tachikawa, N.; Forsyth, M.; Pringle, J. M.; Howlett, P. C.; Elliott, G. D.; Davis, J. H.; Watanabe, M.; Simon, P.; Angell, C. A., Energy Applications of Ionic Liquids. *Energy Environ. Sci.* **2014,** *7*, 232-250.

37. Fukunaga, A.; Nohira, T.; Hagiwara, R.; Numata, K.; Itani, E.; Sakai, S.; Nitta, K.; Inazawa, S., A Safe and High-Rate Negative Electrode for Sodium-Ion Batteries: Hard Carbon in Nafsa-C1c3pyrfsa Ionic Liquid at 363 k. *J. Power Sources* **2014,** *246*, 387-391.

38. Wu, R.; Liu, X.; Zheng, Y.; Li, Y.; Shi, H.; Cheng, X.; Pfleging, W.; Zhang, Y., Unveiling the Intrinsic Reaction between Silicon-Graphite Composite Anode and Ionic Liquid Electrolyte in Lithium-Ion Battery. *J. Power Sources* **2020,** *473*, 228481.

39. Piper, D. M.; Evans, T.; Leung, K.; Watkins, T.; Olson, J.; Kim, S. C.; Han, S. S.; Bhat, V.; Oh, K. H.; Buttry, D. A.; Lee, S.-H., Stable Silicon-Ionic Liquid Interface for Next-Generation Lithium-Ion Batteries. *Nat. Commun.* **2015,** *6*, 6230.

40. Hassoun, J.; Fernicola, A.; Navarra, M. A.; Panero, S.; Scrosati, B., An Advanced Lithium-Ion Battery Based on a Nanostructured Sn–C Anode and an Electrochemically Stable Litfsi-Py24tfsi Ionic Liquid Electrolyte. *J. Power Sources* **2010,** *195*, 574-579.

41. Li, H.; Martha, S. K.; Unocic, R. R.; Luo, H.; Dai, S.; Qu, J., High Cyclability of Ionic Liquid-Produced Tio2 Nanotube Arrays as an Anode Material for Lithium-Ion Batteries. *J. Power Sources* **2012,** *218*, 88-92.

42. Ishikawa, M.; Sugimoto, T.; Kikuta, M.; Ishiko, E.; Kono, M., Pure Ionic Liquid Electrolytes Compatible with a Graphitized Carbon Negative Electrode in Rechargeable Lithium-Ion Batteries. *J. Power Sources* **2006,** *162*, 658-662.

43. Li, Q.; Chen, J.; Fan, L.; Kong, X.; Lu, Y., Progress in Electrolytes for Rechargeable Li-Based Batteries and Beyond. *Green Energy Environ.* **2016,** *1*, 18-42.

44. Wang, Y.; Turk, M. C.; Sankarasubramanian, M.; Srivatsa, A.; Roy, D.; Krishnan, S., Thermophysical and Transport Properties of Blends of an Ether-Derivatized Imidazolium Ionic Liquid and a Li+-Based Solvate Ionic Liquid. *J. Mater. Sci.* **2017,** *52*, 3719-3740.

45. Hwang, J.; Okada, H.; Haraguchi, R.; Tawa, S.; Matsumoto, K.; Hagiwara, R., Ionic Liquid Electrolyte for Room to Intermediate Temperature Operating Li Metal Batteries: Dendrite Suppression and Improved Performance. *J. Power Sources* **2020,** *453*, 227911.

46. Dahbi, M.; Fukunishi, M.; Horiba, T.; Yabuuchi, N.; Yasuno, S.; Komaba, S., High Performance Red Phosphorus Electrode in Ionic Liquid-Based Electrolyte for Na-Ion Batteries. *J. Power Sources* **2017,** *363*, 404-412.

47. Heist, A.; Lee, S.-H., Improved Stability and Rate Capability of Ionic Liquid Electrolyte with High Concentration of Lifsi. *J. Electrochem. Soc.* **2019,** *166*, A1860-A1866.

48. Zhang, H.; Qu, W.; Chen, N.; Huang, Y.; Li, L.; Wu, F.; Chen, R., Ionic Liquid Electrolyte with Highly Concentrated Litfsi for Lithium Metal Batteries. *Electrochim. Acta* **2018,** *285*, 78-85.

49. Wang, F.; Zi, W.; Zhao, B. X.; Du, H. B., Facile Solution Synthesis of Red Phosphorus Nanoparticles for Lithium Ion Battery Anodes. *Nanoscale Res. Lett.* **2018,** *13*, 356.

50. Kim, Y.; Park, Y.; Choi, A.; Choi, N.-S.; Kim, J.; Lee, J.; Ryu, J. H.; Oh, S. M.; Lee, K. T., An Amorphous Red Phosphorus/Carbon Composite as a Promising Anode Material for Sodium Ion Batteries. *Adv. Mater.* **2013,** *25*, 3045-3049.

51. Huang, H.; Xiao, Q.; Wang, J.; Yu, X.-F.; Wang, H.; Zhang, H.; Chu, P. K., Black Phosphorus: A Two-Dimensional Reductant for in Situ Nanofabrication. *npj 2D Mater. Appl.* **2017,** *1*, 20.

52. Franke, R.; Chassé, T.; Streubel, P.; Meisel, A., Auger Parameters and Relaxation Energies of Phosphorus in Solid Compounds. *J. Electron. Spectrosc. Relat. Phenom.* **1991,** *56*, 381-388.

53. Taylor, J. A.; Lancaster, G. M.; Rabalais, J. W., Surface Alteration of Graphite, Graphite Monofluoride and Teflon by Interaction with Ar+ and Xe+ Beams. *Appl. Surf. Sci.* **1978,** *1*, 503-514.

54. Hou, T.; Yang, G.; Rajput, N. N.; Self, J.; Park, S.-W.; Nanda, J.; Persson, K. A., The Influence of Fec on the Solvation Structure and Reduction Reaction of Lipf6/Ec Electrolytes and Its Implication for Solid Electrolyte Interphase Formation. *Nano Energy* **2019,** *64*, 103881.

55. Sodhi, R. N. S.; Cavell, R. G., Kll Auger and Core Level (1s and 2p) Photoelectron Shifts in a Series of Gaseous Sulfur Compounds. *J. Electron. Spectrosc. Relat. Phenom.* **1987,** *42*, 285.

56. Contarini, S.; Rabalais, J. W., Ion Bombardment-Induced Decomposition of Li and Ba Sulfates and Carbonates Studied by X-Ray Photoelectron Spectroscopy. *J. Electron. Spectrosc. Relat. Phenom.* **1985,** *35*, 191-201.

57. Abraham, K. M.; Chaudhri, S. M., The Lithium Surface Film in the Li / So 2 Cell. *J. Electrochem. Soc.* **1986,** *133*, 1307-1311.

58. Luo, X.-F.; Helal, A. S.; Hsieh, C.-T.; Li, J.; Chang, J.-K., Three-Dimensional Carbon Framework Anode Improves Sodiation–Desodiation Properties in Ionic Liquid Electrolyte. *Nano Energy* **2018,** *49*, 515-522.

59. Reinhold, R.; Stoeck, U.; Grafe, H.-J.; Mikhailova, D.; Jaumann, T.; Oswald, S.; Kaskel, S.; Giebeler, L., Surface and Electrochemical Studies on Silicon Diphosphide as Easy-to-Handle

Anode Material for Lithium-Based Batteries—the Phosphorus Path. *ACS Appl. Mater. Interfaces* **2018,** *10*, 7096-7106.

60. Bai, A.; Wang, L.; Li, J.; He, X.; Wang, J.; Wang, J., Composite of Graphite/Phosphorus as Anode for Lithium-Ion Batteries. *J. Power Sources* **2015,** *289*, 100-104.

61. Nagao, M.; Hayashi, A.; Tatsumisago, M., All-Solid-State Lithium Secondary Batteries with High Capacity Using Black Phosphorus Negative Electrode. *J. Power Sources* **2011,** *196*, 6902-6905.

Graphical abstract